Warsaw University of Technology

FACULTY OF
ELECTRONICS AND INFORMATION TECHNOLOGY



Institute of Faculty of Power and Aeronautical Engineering

Bachelor's diploma thesis

in the field of study Aerospace Engineering
and specialisation Aerospace Engineering

Aerodynamic Performance Analysis of a Starship rocket

Kacper Frelek
student record book number 313668

thesis supervisor
MEng Michał Klamka

WARSAW 2025

Contents

Nomenclature . . . 6
1. Introduction . . . 7
2. Starship vehicle . . . 8
3. Aim of the project . . . 10
4. Geometry . . . 11
5. Meshing . . . 11
5.1. Mesh Sensitivity Studies . . . 13
6. Fluent Settings . . . 15
6.1. Superposition of Fins and Canards . . . 16
7. Computational Fluid Dynamics . . . 18
7.1. Governing Equation . . . 18
7.2. Turbulence Models . . . 19
7.2.1. RANS . . . 19
7.2.2. SST k–ω Turbulence Model . . . 20
8. Computational Fluid Dynamics -simulation cases . . . 21
9. Results . . . 22
10. Conclusions . . . 25
11. Summary . . . 26
11.1. Analysis Summary . . . 26
11.2. Future Work . . . 26
References . . . 28
List of Figures . . . 29
List of Tables . . . 29
List of Appendices . . . 29

Aerodynamic Performance Analysis of Starship reentry

Abstract.
Reducing costs and minimizing turnaround times have become central goals in the modern aerospace industry. SpaceX's Starship, with its fully reusable architecture, exemplifies this shift by integrating aerodynamic innovations that enhance reentry performance while lowering operational expenses. This thesis focuses on the aerodynamic aspects of Starship's reentry, examining how its shape, control surfaces, and flight maneuvers contribute to both efficient energy management and structural integrity during descent. By optimizing aerodynamic control through techniques such as body flaps and controlled descent profiles, Starship minimizes the need for extensive post-flight repairs and inspections, thereby reducing both time and financial costs. Computational Fluid Dynamics (CFD) simulations and real-world flight data are employed to analyze airflow patterns, drag coefficients, and aerodynamic heating, offering insights into how these factors contribute to the overall cost-effectiveness of reusable spacecraft.

Keywords: Starship, reentry, aerodynamics, cost efficiency, time optimization, Computational Fluid Dynamics, reusability.

Analiza Wydajności Aerodynamicznej Starshipa

Streszczenie.
Obniżenie kosztów i minimalizacja czasu przygotowania misji stały się kluczowymi celami we współczesnym przemyśle kosmicznym. Starship firmy SpaceX, dzięki swojej w pełni wielokrotnego użytku architekturze, jest przykładem tej zmiany poprzez integrację innowacji aerodynamicznych, które poprawiają wydajność podczas wejścia w atmosferę, jednocześnie obniżając koszty operacyjne. Niniejsza praca koncentruje się na aspektach aerodynamicznych wejścia Starshipa do atmosfery, badając, w jaki sposób jego kształt, powierzchnie sterujące i manewry lotu przyczyniają się do efektywnego zarządzania energiią oraz zachowania integralności strukturalnej podczas opadania. Optymalizując kontrolę aerodynamiczną poprzez techniki takie jak klapy kadłuba i kontrolowane profile opadania, Starship minimalizuje potrzebę rozległych napraw i inspekcji po locie, co prowadzi do redukcji zarówno czasu, jak i kosztów finansowych. Symulacje Dynamiki Płynów Obliczeniowych (CFD) oraz dane z rzeczywistych lotów są wykorzystywane do analizy wzorców przepływu powietrza, współczynników oporu i nagrzewania aerodynamicznego, dostarczając wglądu w to, jak te czynniki wpływają na ogólną efektywność kosztową statków kosmicznych wielokrotnego użytku.

Słowa kluczowe: Starship, wejście w atmosferę, aerodynamika, efektywność kosztowa, optymalizacja czasu, Dynamika Płynów Obliczeniowych, ponowne użycie.

Nomenclature

- CFD - computational Fluid Dynamics
- FEM - Finite Elements Method
- $M*$ - local Mach speed
- U_∞ - local velocity
- c- local speed of sound
- ρ_∞ = freestream density
- V_∞ = freestream velocity
- μ_∞ = freestream dynamic viscosity
- ν_∞ - freestream kinematic viscosity
- ρ - density of fluid
- Ξ - stress tensor field
- I - identity matrix
- $\otimes$ - tensor produt
- $\mathbf{v}$ - velocity matrix
- $\frac{\partial}{\partial t}$ - partial derivative with respect to time
- ∇ - Nabla Operator
- $\frac{D}{Dt}$ - total derivative with respect to time
- γ_h - mass-specific density of internal heat sources
- δ - heat conduction coefficient of the medium
- f - force field
- A - reference area

1. Introduction

In recent years, the aerospace industry has undergone significant transformations, focusing on optimizing mission costs and turnaround times through the development of reusable technologies. SpaceX, as a leader in this shift, introduced Starship—a spacecraft designed for repeated atmospheric reentries and landings with minimal maintenance requirements. A critical component of Starship's (Fig: 1.1) efficiency lies in its aerodynamic properties, which play a decisive role in energy management during Earth reentry.

The primary objective of this thesis is to analyze the aerodynamic performance of Starship during atmospheric reentry at various angles of attack (AOA) and different configurations of flaps and canards. Understanding how these variables influence aerodynamic forces, moments, and vehicle stability is essential for optimizing reentry trajectories and minimizing structural loads.

Advanced simulation methods, including Computational Fluid Dynamics (CFD), are utilized to model airflow around the vehicle under different configurations. The analysis also compares simulation results with real-world flight test data, enabling validation of theoretical models. The findings provide valuable insights into optimal control surface settings that reduce drag, manage aerodynamic heating, and ensure a safe and efficient return.

This work contributes to the advancement of reusable space technologies by offering a detailed aerodynamic analysis that can be applied to further optimize future spacecraft designs.

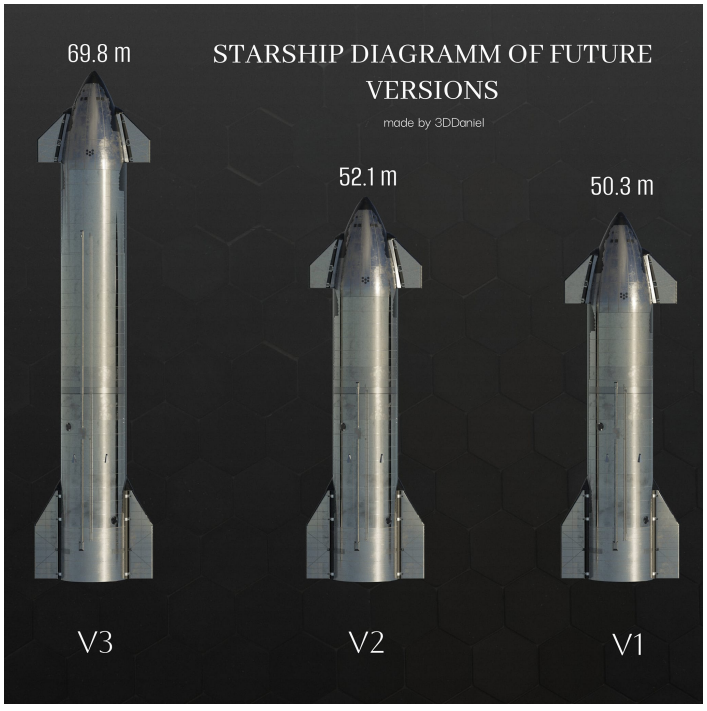


Figure 1.1. Starship rocket configurations with future plans to develope

2. Starship vehicle

Starship is SpaceX's fully reusable spacecraft, designed to carry both crew and cargo to a variety of destinations, including low Earth orbit, the Moon, Mars, and beyond. Initially introduced as a prototype, Starship has undergone several iterations, each incorporating lessons learned from previous test flights to enhance its performance and reliability.

The first model of Starship, which is the primary focus of this thesis, featured a stainless-steel body with a distinctive aerodynamic shape optimized for both atmospheric reentry and space travel. It includes four large, actuating control surfaces—two forward canards near the nose and two aft flaps near the base. These surfaces are crucial for managing the vehicle's orientation and stability during the high-speed reentry phase, allowing Starship to perform controlled descents and landings.

Since the initial model, Starship has seen significant advancements in both design and performance. Improvements have been made to its heat shield, structural integrity, and aerodynamic efficiency. The latest iterations of Starship continue to refine the balance between aerodynamic control and thermal protection, demonstrating SpaceX's commitment to continuous innovation.

The control surfaces of Starship play a pivotal role in its reentry strategy. By adjusting the angles of the forward canards and aft flaps, the spacecraft can alter its angle of attack, modulate drag forces, and control its descent trajectory. This capability is essential for achieving precise landings and minimizing aerodynamic stresses on the structure.

Understanding the aerodynamic behavior of these control surfaces under various conditions (2.1) is critical for optimizing reentry performance. This thesis focuses on analyzing the aerodynamic forces and moments generated by different control surface configurations, contributing to the broader goal of enhancing the reusability and cost-efficiency of Starship and similar future spacecraft.



Figure 2.1. Starship rocket damaged fin closeup

3. Aim of the project

The primary aim of this thesis is to conduct a comprehensive CFD analysis of Starship's aerodynamic performance during atmospheric reentry. The focus is on evaluating how varying AOA influences aerodynamic forces, stability, and overall reentry efficiency.

By simulating multiple reentry scenarios with different AOA and control surface angles, this research seeks to identify optimal aerodynamic configurations that minimize drag, control aerodynamic heating, and maintain structural stability. These simulations are essential for understanding the complex airflow patterns and pressure distributions that occur during high-speed reentry, which directly affect Starship's descent trajectory and landing precision.

An additional aim of this thesis is to investigate whether counterposition configurations of the fins and canards can be used to interpolate aerodynamic behavior for standard configurations. For example, it will be examined if a setup with a fin angle of -60 degrees and a canard angle of 60 degrees yields similar aerodynamic characteristics to a configuration where both fin and canard are set at 60 degrees. This approach, if validated, could significantly reduce the number of simulations required, thereby saving computational resources and time.

4. Geometry

The geometry (4.1) used for this analysis is based on the first prototype model of SpaceX's Starship. The 3D model includes the main fuselage, forward canards, and aft flaps, each accurately representing their dimensions and placement relative to the vehicle's center of mass. The body is modeled as a stainless-steel cylindrical structure with a rounded nose cone and tapered tail section, characteristic of the original Starship design.

The canards are located near the nose of the vehicle, designed to provide pitch control during reentry. The aft flaps are positioned at the base and are responsible for modulating drag and stability. These control surfaces are modeled with full rotational capabilities to simulate various angles of deflection. Simplifications were made to exclude minor surface details, focusing instead on key aerodynamic structures that influence reentry performance.

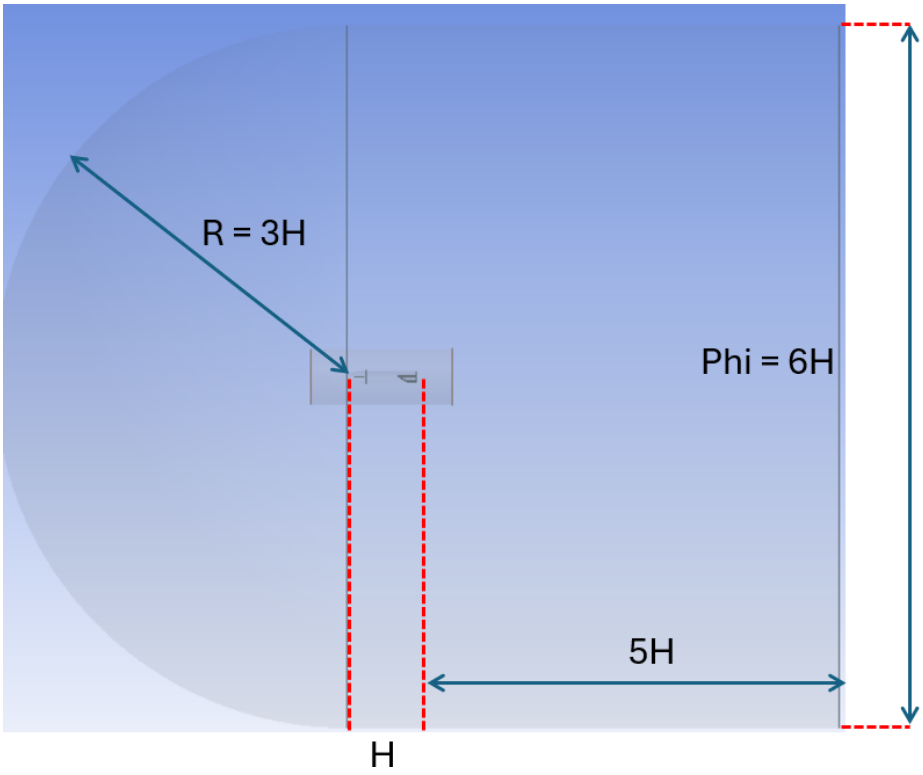


Figure 4.1. Analyzed domain

5. Meshing

The meshing process is a critical step in ensuring accurate CFD analysis. A hybrid mesh was generated, combining structured and unstructured elements to balance computational efficiency with solution accuracy (5.1).

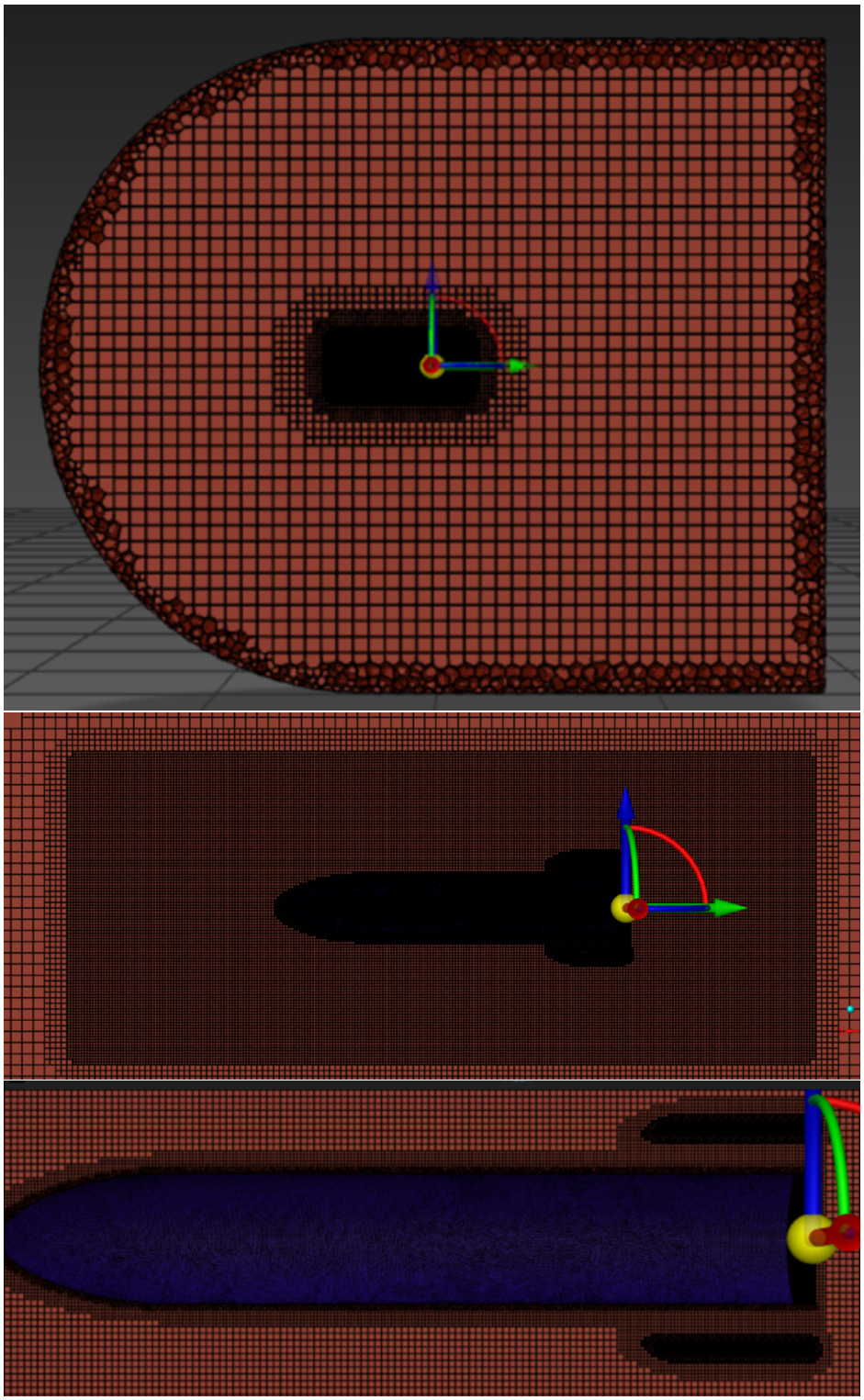


Figure 5.1. Mesh created for the model

The regions near the control surfaces and the vehicle's body, where high gradients in flow properties are expected, were refined with a denser mesh (5.2) to capture detailed aerodynamic phenomena.

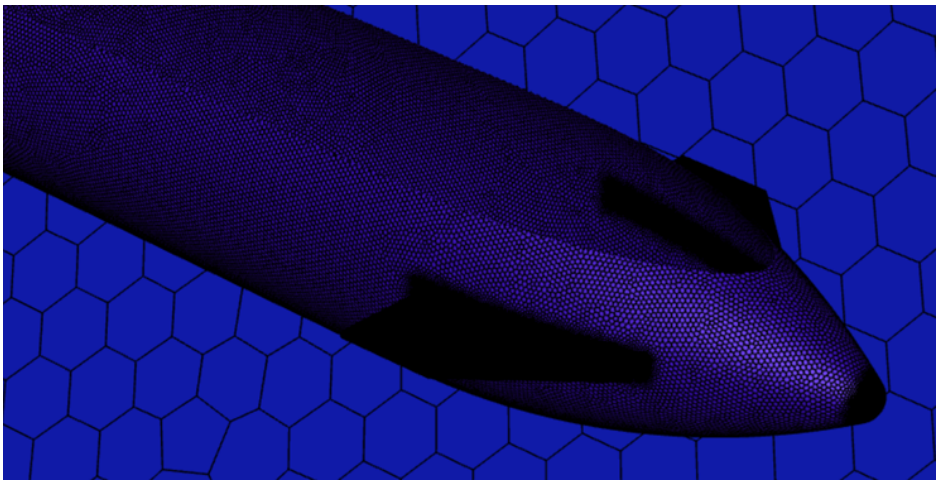


Figure 5.2. Denser mesh on cannards

Inflation layers were added around the fuselage and control surfaces to accurately resolve boundary layer effects. The far-field boundary conditions were extended sufficiently to prevent any interference from the domain edges, ensuring that the flow around the vehicle is undisturbed.

Mesh independence tests were conducted to verify that the solution accuracy is not significantly affected by further mesh refinement. The final mesh configuration provided a balance between computational cost and the precision required for reliable aerodynamic analysis.

5.1. Mesh Sensitivity Studies

To ensure the reliability of the CFD results, a mesh sensitivity study was conducted. Multiple mesh densities were tested, ranging from coarse to fine grids, to assess their impact on key aerodynamic parameters such as drag coefficient, lift, and pressure distribution.

The study involved comparing results from different mesh configurations to determine at which point further refinement no longer produced significant changes in the outcomes. It was found that beyond a certain mesh density, the variations in aerodynamic coefficients were minimal, indicating that the solution had reached mesh independence.

This process validated the chosen mesh configuration, ensuring that the results presented in this thesis are both accurate and computationally efficient. The findings from the mesh sensitivity study also highlight the importance of balancing mesh quality with resource limitations, particularly in complex simulations involving high-speed reentry scenarios.

Based on the results from the mesh sensitivity studies presented in Table 5.1, the Finest mesh configuration, consisting of 15.5 million cells, was selected for the final simulations. This decision was driven by a careful balance between solution accuracy

	Coarse	Mid	Finest	Finestv2	Avg from 4	Avg from 3
C_d	0.8455	0.8639	0.7885	0.7919	0.8224	0.8148
% err to 4	3%	5%	-4%	-4%		
% err to 3	–	6%	-3%	-3%		
Mln #cells	7.22	11.61	15.50	16.34		

Table 5.1. Simulation results with different mesh resolutions.

and computational efficiency, ensuring reliable results without incurring unnecessary computational costs.

The Finest mesh demonstrated a minimal error margin when compared to the more refined Finestv2 mesh. The drag coefficient (C_d) obtained from the Finest mesh was 0.7885, while the Finestv2 yielded a C_d of 0.7919, representing only a 0.4

Choosing the Finest mesh provided several advantages:

- **Computational Efficiency:** The Finest mesh required fewer computational resources compared to the Finestv2 mesh, leading to reduced simulation time and lower hardware demands. This efficiency was particularly important given the complex nature of high-speed reentry simulations, where numerous iterations and parametric studies were necessary.
- **Accuracy Assurance:** Despite the reduced cell count relative to *Finestv2*, the *Finest* mesh maintained high accuracy, as evidenced by the minor differences in aerodynamic coefficients.
- **Mesh Independence:** The small variations in C_d and other aerodynamic parameters between the *Finest* and *Finestv2* meshes confirmed that the solution had reached mesh independence. This validation ensured that the final results were not influenced by further mesh refinement, adding confidence to the conclusions drawn from the simulations.

In summary, the selection of the Finest mesh with 15.5 million cells offered an optimal compromise between computational cost and the accuracy (5.3) required for the objectives of this study. This approach allowed for a detailed investigation of the Starship's aerodynamic and thermal performance during reentry, while maintaining efficient use of computational resources.

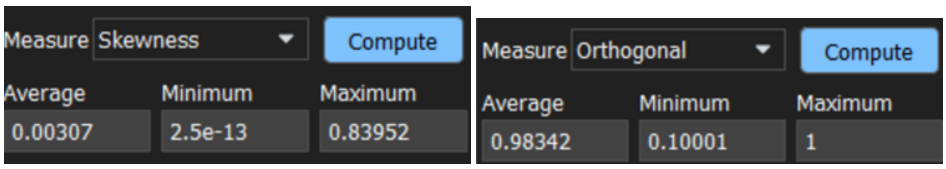


Figure 5.3. Skewness and orthogonality of the mesh

6. Fluent Settings

The CFD simulations were carried out using ANSYS Fluent. The solver settings were configured to handle high-speed compressible flow, typical of atmospheric reentry conditions. The following key settings were applied:

- Solver Type: Density-based solver for accurate resolution of compressible flow.
- Turbulence Model: k-ω SST (Shear Stress Transport) model was used to capture both laminar and turbulent flow characteristics.
- Boundary Conditions: The far-field boundaries were set with atmospheric reentry conditions, while the vehicle surfaces were treated as no-slip walls with adiabatic heat transfer assumptions.
- Discretization: Second-order upwind schemes were employed for spatial discretization to enhance solution accuracy.
- **Convergence Criteria:** Residuals for continuity, momentum, and energy equations were monitored, with convergence achieved when residuals dropped to sufficiently steady level (6.1).

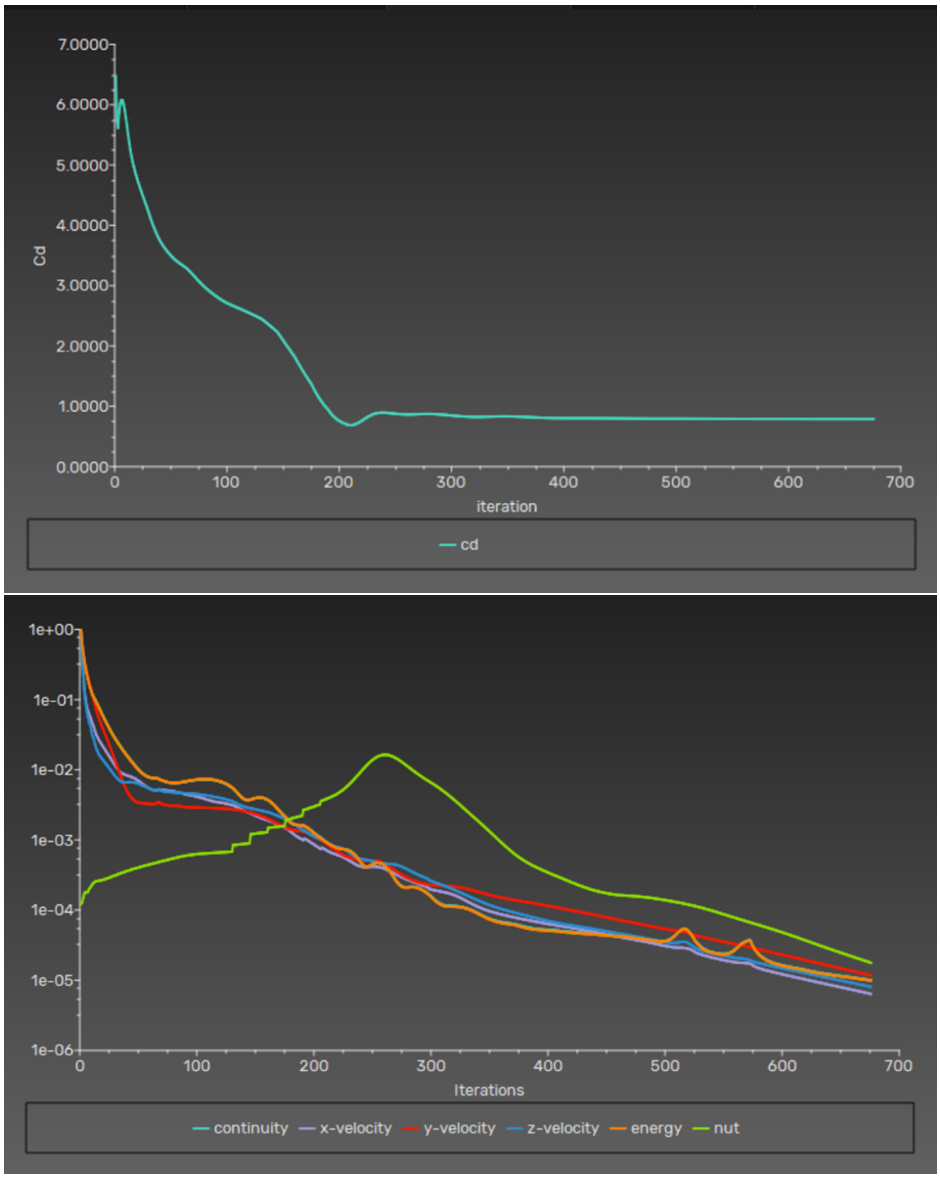


Figure 6.1. Convergence of residuals and drag coefficient

6.1. Superposition of Fins and Canards

An additional aspect of this thesis involves examining the superposition principle in the context of Starship's aerodynamic control surfaces. Specifically, this study investigates whether the aerodynamic effects of the forward canards and aft fins can be considered additive, allowing for simplified interpolation between different control surface configurations.

To test this hypothesis, simulations were conducted for configurations with opposing angles of canards and fins. For example, scenarios with a fin angle of $-60°$ and a canard angle of $60°$ (denoted as *f60r60*) were compared against configurations where the fin was set to $60°$ and the canard to $-60°$ (denoted as *fn60r60*). The aerodynamic coefficients

obtained from these simulations were analyzed to assess the validity of the superposition approach.

Configuration	Canard	Fin	Error (Fin)	Error (Canard)
f60r60	-0.10596	-0.01989	10%	-15%
fn60r60	-0.11698	-0.01693		

Table 6.1. Comparison of aerodynamic coefficients for opposing fin and canard angles.

The results, summarized in Table 6.1, demonstrate that the aerodynamic coefficients for both the canards and fins are consistent with the expectations of the superposition principle. The canard coefficient for the *f60r60* configuration is -0.10596, while for the *fn60r60* configuration, it is -0.11698. Similarly, the fin coefficients are -0.01989 and -0.01693, respectively.

The error associated with the fin coefficient is approximately 10%, while the canard coefficient shows an error of -15%. These error values are within acceptable ranges for computational fluid dynamics simulations, considering the inherent complexities of high-speed aerodynamic modeling and the approximations involved in mesh generation and numerical solvers. The acceptable error margins suggest that the superposition of aerodynamic effects from canards and fins provides a reasonably accurate method for predicting overall aerodynamic behavior.

These findings support the potential for using simplified superposition models in future analyses, reducing computational effort without significantly compromising accuracy. This approach could streamline the design and testing process for reusable spacecraft, facilitating more efficient exploration of control surface configurations and improving the cost-effectiveness of aerodynamic optimization.

7. Computational Fluid Dynamics

7.1. Governing Equation

One can define three equations that define the fundamental laws of fluid behaviour. They describe the conservation of mass, momentum and energy of a fluid. First of them, also called continuity equation [Eq. 1], says that mass can't just vanish into thin air or appear from nowhere. In any fluid system, the mass flowing in must either flow out or accumulate, where this equation can be simplified for an incompressible flow [Eq. 2].

$$\frac{\delta \rho}{\delta t} + \nabla(\rho \vec{v}) = 0 \tag{1}$$

$$\nabla \cdot \vec{v} = 0 \tag{2}$$

The second equation defining conservation of momentum says that the rate of change of momentum equals the forces acting on the fluid. It is a form of Newton's second law for fluid mechanics. For compressible flows, it takes the form of [Eq. 3]. A common simplification in low-speed aerodynamics allows the use of an incompressible form of this equation, where viscosity can be assumed to be a constant value. Thus, the equation takes the form of [Eq. 4].

$$\rho\left(\frac{\partial \vec{v}}{\partial t} + (\vec{v} \cdot \nabla)\vec{v}\right) = -\nabla p + \nabla \cdot \boldsymbol{\tau} + \rho \vec{f} \tag{3}$$

$$\rho\left(\frac{\partial \vec{v}}{\partial t} + (\vec{v} \cdot \nabla)\vec{v}\right) = -\nabla p + \mu \nabla^2 \vec{v} + \rho \vec{f} \tag{4}$$

The third of the fundamental equations that define fluid mechanics is the energy equation. It describes how a fluid's total energy (including internal, kinetic, and sometimes potential energy) changes due to heat transfer, work done by pressure and viscous forces, and external body forces. It's the fluid-dynamics version of the First Law of Thermodynamics, governing how temperature and energy evolve within a flow. In compressible flow, the energy equation [Eq. 5] includes pressure work and compression heating, making it dependent on changes in density and internal energy, while in incompressible flow [Eq. 6], those terms drop out, reducing the equation to a heat transport equation driven by conduction and convection.

$$\frac{\partial}{\partial t}(\rho e_t) + \nabla \cdot (\rho e_t \vec{v}) = -\nabla \cdot \vec{q} + \nabla \cdot (\boldsymbol{\tau} \cdot \vec{v}) + \rho \vec{f} \cdot \vec{v} \tag{5}$$

$$\rho c_p \left(\frac{\partial T}{\partial t} + \vec{v} \cdot \nabla T\right) = k \nabla^2 T + \Phi \tag{6}$$

7.2. Turbulence Models

Because the Navier-Stokes equations for turbulent flows span a wide variety of spatial and temporal scales, their direct solution is computationally impossible in real-world computational fluid dynamics (CFD) applications. In order to address this issue, turbulence models are presented in order to approximate how the mean flow is affected by the unresolved turbulent fluctuations.

This can be accomplished by employing Reynolds averaging to separate the flow variables into mean and fluctuating components. Reynolds stresses, which indicate momentum transfer brought on by turbulence, are extra terms that emerge as a result of the process. These new terms cause the system to become unclosed, which is a problem known as the closure problem, because they add more unknowns than equations.

By expressing the Reynolds stresses in terms of known modelled quantities, like eddy viscosity concept, turbulence models can be used to provide closure. It is done by using various turbulence models like Spallart-Almaras, k-ϵ, and k-ω to solve additional transport equations for turbulent properties, like turbulent kinetic energy, to approximate Reynolds stresses. This approach allows the modified Reynolds-averaged Navier–Stokes (RANS) equations to be solved efficiently for the mean flow field.

7.2.1. RANS

RANS approach is a numerical method that is based on decomposing flow quantities (like velocity and pressure) into their time-averaged and fluctuating components to model a turbulent flow. Most of these models are based on empirical observations.

$$u(x,t) = \overline{u}(x) + u'(x,t) \tag{7}$$

$$\overline{u} = \frac{1}{\Delta t}\int_{t}^{t+\Delta t} u_i \, dt \tag{8}$$

The governing equations for the mean flow variables are obtained by applying Reynolds averaging to the Navier-Stokes equations. But the momentum equation also contains other unknown terms, the Reynolds stresses, which need to be modelled in order to be closed. The momentum equation for incompressible flow looks like this:

$$\rho\left(\frac{\partial \overline{\vec{v}}}{\partial t} + \overline{\vec{v}}\cdot\nabla\overline{\vec{v}}\right) = -\nabla\overline{p} + \mu\nabla^2\overline{\vec{v}} - \nabla\cdot\left(\rho\,\overline{\vec{v}'\vec{v}'}\right) \tag{9}$$

The term $\rho\overline{\vec{v}'\vec{v}'}$ is called the Reynolds stress tensor, which must be modelled to close the system of equations. In order to do that, the Boussinesq approximation [1] is applied. It allows for modelling Reynolds stresses, as it introduces the concept of turbulent eddy viscosity μ_t.

$$-\rho\overline{v_i' v_j'} = \mu_t\left(\frac{\partial \overline{v}_i}{\partial x_j} + \frac{\partial \overline{v}_j}{\partial x_i}\right) - \frac{2}{3}\rho k\delta_{ij} \tag{10}$$

Here, $k = \frac{1}{2}\overline{v_i' v_i'}$ is the turbulent kinetic energy. This approximation enables the use of turbulence models to calculate μ_t.

Similarly, one can present RANS equations for compressible flow, as they differ from the incompressible ones. In compressible turbulent flows, the Reynolds averaging is applied to all flow variables, including density, velocity, pressure, and total energy. The Favre-averaging [2] technique is often used for thermodynamic variables, where a density-weighted average is applied. The decompositions are as follows:

$$\phi = \tilde{\phi} + \phi'', \quad \text{where} \quad \tilde{\phi} = \frac{\overline{\rho\phi}}{\overline{\rho}} \tag{11}$$

Here, $\tilde{\phi}$ represents the Favre-averaged variable, which can be any dependent variable and ϕ'' its fluctuation.

$$\frac{\partial(\overline{\rho}\tilde{\vec{v}})}{\partial t} + \nabla\cdot(\overline{\rho}\tilde{\vec{v}}\otimes\tilde{\vec{v}}) = -\nabla\overline{p} + \nabla\cdot\left[(\mu+\mu_t)\left(\nabla\tilde{\vec{v}} + \nabla\tilde{\vec{v}}^T - \frac{2}{3}\nabla\cdot\tilde{\vec{v}}\,\mathbb{I}\right)\right] \tag{12}$$

$$\frac{\partial(\overline{\rho}\tilde{e}_t)}{\partial t} + \nabla\cdot\left(\overline{\rho}\tilde{e}_t\tilde{\vec{v}}\right) = \nabla\cdot\left[(\lambda+\lambda_t)\nabla\tilde{T}\right] + \nabla\cdot\left[\tilde{\vec{v}}\cdot(\boldsymbol{\tau}+\boldsymbol{\tau}_t)\right] \tag{13}$$

Here, $\tilde{e}_t$ is the Favre-averaged total energy per unit mass, λ_t is the turbulent thermal conductivity, and $\boldsymbol{\tau}_t$ is the turbulent stress tensor derived using the eddy viscosity model.

$$\vec{q}_t = -\frac{\mu_t c_p}{Pr_t}\nabla\tilde{T} \tag{14}$$

7.2.2. SST k–ω Turbulence Model

The Shear Stress Transport (SST) k-ω model combines the advantages of the k-ω model near walls with the k-ϵ model in the free stream. It uses blending functions to switch between these models based on distance from the wall and local flow properties. To model turbulent kinetic energy, the model uses Eq. 15 and for specific dissipation rate Eq. 16.

$$\frac{\partial(\rho k)}{\partial t} + \nabla\cdot(\rho k\vec{v}) = \nabla\cdot\left[\left(\mu+\sigma_k\mu_t\right)\nabla k\right] + P_k - \beta^*\rho k\omega \tag{15}$$

$$\frac{\partial(\rho\omega)}{\partial t} + \nabla\cdot(\rho\omega\vec{v}) = \nabla\cdot\left[\left(\mu+\sigma_\omega\mu_t\right)\nabla\omega\right] + \alpha\frac{\omega}{k}P_k - \beta\rho\omega^2 + 2(1-F_1)\frac{\rho\sigma_{\omega 2}}{\omega}\nabla k\cdot\nabla\omega \tag{16}$$

Here, F_1 is a blending function that activates the near-wall behaviour of the model. Constants like α, β, σ_k are typically calibrated based on experimental data for aerodynamic flows, but for most solvers, they are predefined and can be checked in manuals.

8. Computational Fluid Dynamics -simulation cases

To analyze the aerodynamic performance of Starship during reentry, a range of Mach numbers was selected to capture various flow regimes. The chosen cases cover hypersonic, supersonic, transonic, and subsonic conditions, ensuring a comprehensive evaluation of aerodynamic behavior across different flight phases. The selection avoids excessively large variations between consecutive Mach numbers to maintain consistency in interpolation and trend analysis.

The table below presents the key flow parameters at different Mach numbers, including density, Reynolds number, dynamic viscosity, altitude, velocity, temperature, dynamic pressure, and atmospheric pressure.

Table 8.1. Flow conditions for selected Mach numbers

Mach [-]	ρ **[kg/m^3]**	**Re [-]**	**Dyn. Visc. [Pa s] e-5**	**Alt. [km]**	**Vel [km/h]**	**U [m/s]**	**T [K]**	**Dyn. Pres. [P]**	**Pressure [Pa]**
4.05	7.23E-04	7.58E+06	6.34	35	4510	1252.78	238.55	567.4	674
2.55	9.68E-04	6.81E+06	5.80	30	2770	769.44	228.15	286.5	1130
1.85	1.21E-03	6.31E+06	5.64	27	2000	555.56	225.15	186.7	1530
1.63	1.40E-03	6.51E+06	5.54	25	1750	486.11	223.15	165.4	2090
1.12	1.70E-03	5.57E+06	5.40	22	1200	333.33	220.15	94.4	3330
1.03	2.05E-03	6.27E+06	5.30	20	1100	305.56	218.15	95.7	5470
0.82	3.14E-03	7.60E+06	5.29	17	870	241.67	218.00	91.7	8790
0.69	5.55E-03	1.14E+07	5.24	14	730	202.78	217.00	114.1	14100
0.60	9.35E-03	1.68E+07	5.24	11	640	177.78	217.00	147.8	22600
0.51	0.526	6.98E+08	6.21	8	560	155.56	236.20	6364.0	35651
0.39	0.819	7.25E+08	7.65	4	460	127.78	262.20	6686.0	61660
0.31	1.112	6.86E+08	8.84	1	370	102.78	281.70	5873.2	89876

The selection of these cases allows for an in-depth study of the aerodynamic forces and moments acting on Starship across different speeds and altitudes. Furthermore, it provides the basis for analyzing how control surfaces such as fins and canards behave in various configurations and angles of attack.

9. Results

In this section, we present and discuss the outcomes of the CFD simulations conducted for Starship's atmospheric reentry. The focus is primarily on evaluating the force coefficients and moment coefficients, which are critical for understanding the aerodynamic performance and stability of the spacecraft.

Specifically, we analyse how variations in angle of attack and control surface configurations affect:

- **Force Coefficients:** Including drag and lift coefficients, which quantify the aerodynamic forces acting on the vehicle.
- **Moment Coefficients:** Pitching moment coefficient, which provides insight into the vehicle's stability and control.

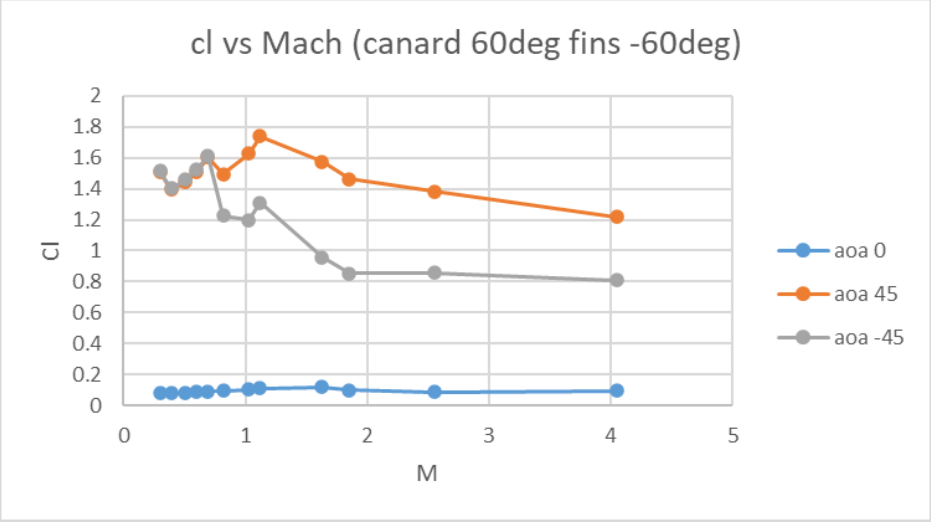


Figure 9.1. Lift coefficient vs Mach graph

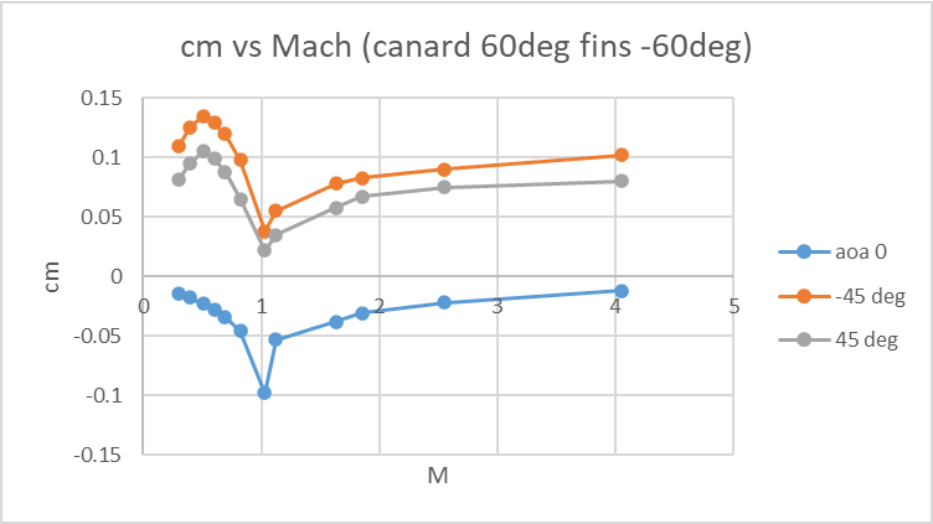


Figure 9.2. Moment coefficient vs Mach graph

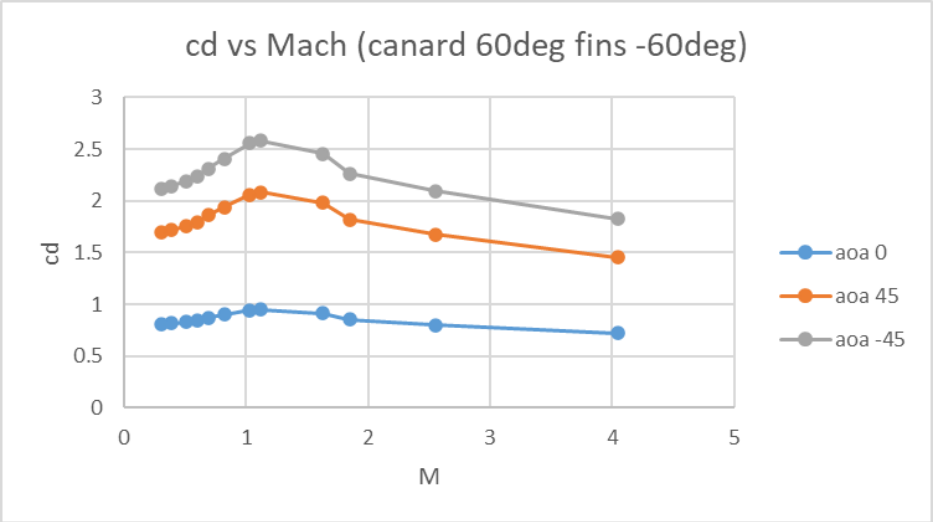


Figure 9.3. Drag coefficient vs Mach graph

These coefficients are central to predicting the behaviour of Starship during reentry. The study evaluates the trends observed across different Mach regimes and validates the CFD results against available experimental data. By comparing configurations—such as those employing counterposition of fins and canards with standard configurations—we assess whether simplified interpolation methods can be reliably applied.

As shown in Figure 9.1, the lift coefficient increases steadily in the subsonic regime and then undergoes a pronounced rise as the free-stream Mach number transitions through M≈0.8-1.2, reaching its peak just above M=1.1. Beyond this transonic spike, the lift coefficient gradually declines and stabilises at a lower, nearly constant value in the supersonic and hypersonic regimes, M>2, demonstrating that the body-flap and canard

configuration provides maximum lift augmentation immediately before Mach 1, followed by a more predictable lift behaviour at higher speeds.

The drag coefficient C_D, depicted in Figure 9.3, exhibits the classic transonic drag rise, with a sharp maximum between $M = 0.9$ and 1.1, before decreasing as Mach number increases further. In subsonic flight C_D remains low and nearly constant, whereas the transonic region incurs the greatest drag penalty—and thus the highest heating and deceleration loads. Once in the fully supersonic regimes ($M > 2$), shock-induced drag effects moderate, and C_D diminishes, indicating a more aerodynamically "forgiving" regime for sustained high-speed descent.

Figure 9.2 illustrates the pitching-moment coefficient C_m, which is slightly negative at low Mach numbers (nose-down stability) and becomes more negative through the transonic window ($M \approx 1.0$) due to shock-induced shifts in pressure distribution. As the flow accelerates into the supersonic and hypersonic regimes, C_m drifts back toward neutral, implying that Starship attains a balanced trim and requires progressively less control-surface deflection to maintain stable flight.

Taken together, these three Mach-sweep trends identify the critical phases in which active control-surface management is most necessary. During transonic passage, lift augmentation, drag mitigation, and counteracting nose-down pitching moments must be expertly balanced—demanding maximum body-flap and canard authority—while the supersonic and hypersonic regimes allow for reduced control inputs as aerodynamic coefficients converge toward steadier values. This comprehensive characterization underpins the development of optimized reentry control strategies for reusable launch vehicles.

Key aerodynamic insights from these results include the pronounced lift surge around Mach 1.0–1.2—which underscores the necessity of precise flap and canard deflections to maximize lift without inducing flow separation—and the corresponding drag spike at $M \approx 0.9$–1.1, which marks the worst-case heating and deceleration loads before a steady reduction in drag for $M > 2$. Additionally, the deepest nose-down pitching moment in the transonic region highlights the requirement for active control inputs to maintain trim, whereas the trend of C_m returning toward neutral at higher Mach numbers predicts a self-trimming behaviour that eases control demands. In the supersonic regime, both C_L and C_D exhibit relative stability for $M > 2$, forecasting a predictable aerodynamic performance window ideal for sustained high-speed manoeuvres. Finally, in the hypersonic regime minimal variation in all three coefficients suggests that trim settings established post-transonic can be maintained with only minor adjustments, supporting efficient and robust reentry control.

10. Conclusions

The CFD analysis conducted in this thesis has provided a comprehensive understanding of Starship's aerodynamic behavior across a broad Mach number range, from subsonic through hypersonic conditions. First, the lift coefficient C_L exhibits a pronounced transonic spike between $M \approx 0.8$ and 1.2, peaking just above Mach1, before declining to a lower, stable value at higher speeds. This confirms that the body-flap and canard configuration delivers maximum lift augmentation immediately after the transonic transition, then transitions into a predictable supersonic lift regime. Second, the drag coefficient C_D shows the characteristic transonic drag rise, with its maximum between $M = 0.9$ and 1.1, followed by a steady decrease for $M > 2$. This behavior identifies the transonic window as the most thermally and structurally demanding phase of reentry, while the supersonic and hypersonic regimes present a more "forgiving" aerodynamic environment. Third, the pitching-moment coefficient C_m is slightly negative at low Mach, intensifies nose-down stability through the transonic region, and returns toward neutral in the supersonic and hypersonic regimes, indicating a natural trend toward self-trim at high speeds.

The mesh sensitivity study confirmed that a 15.5million-cell mesh achieves mesh independence with less than a 0.5% difference in drag coefficient compared to an even finer grid, thus balancing accuracy and computational efficiency. In addition, superposition tests of opposing fin and canard deflections demonstrated acceptable error margins (10% for fin coefficients and 15% for canard coefficients), validating the use of additive modeling to interpolate control-surface effects. This approach lays the groundwork for rapidly assessing a wide range of flap and canard angle combinations—along with their impact on all aerodynamic coefficients and shifts in the center of pressure—without the need for exhaustive individual simulations.

Due to computational time and resource constraints, only one representative control-surface configuration was simulated in detail for the full Mach sweep. However, the validated superposition principle means that future work can confidently explore multiple flap and canard settings, predict their combined effects on lift, drag, moment coefficients, and center-of-pressure locations, and refine reentry trim strategies more efficiently.

Overall, these results validate the aerodynamic performance and stability characteristics of Starship's reentry control surfaces and define the regions where active control input is most critical. The sharp lift and drag variations in the transonic regime underscore the need for precise body-flap and canard deflections to manage loads and heating, while the convergence of all three coefficients in the supersonic and hypersonic regimes suggests that control strategies can transition to more open-loop or self-trimming schemes. These insights establish a foundation for optimized reentry guidance laws and inform future design refinements aimed at reducing maintenance turnaround and operational costs for fully reusable launch vehicles.

11. Summary

11.1. Analysis Summary

This work presented a detailed CFD investigation of Starship's reentry configuration, with an emphasis on the interplay between body flaps and canards across subsonic, transonic and hypersonic regimes. A high-fidelity 15.5 M-cell mesh—validated through mesh-independence tests—was used to capture shock-wave structures (Fig. 11.1) and boundary-layer behaviour. Simulations at Mach numbers spanning 0.8 to 4.05 revealed the characteristic lift surge and drag rise in the transonic window, as well as the subsequent stabilization of aerodynamic coefficients in supersonic and hypersonic flow. A targeted superposition study confirmed that opposing finite and canard deflections can be combined additively with less than 15 % error, enabling rapid interpolation of control-surface effects without full re-runs. The pitching-moment trends closely tracked center-of-pressure shifts, highlighting the need for active trim during Mach 0.9–1.2 and indicating a transition to near-self-trim in high-speed flight.

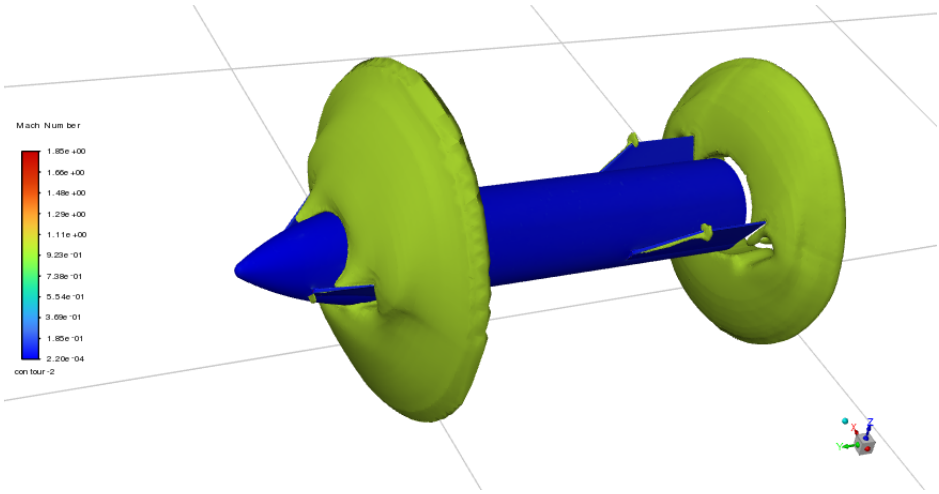


Figure 11.1. Iso-Surface AoA-0deg fin60deg canard60deg M=1.81

11.2. Future Work

Building on these findings, future efforts should leverage the validated superposition approach to explore a broader matrix of flap and canard angles, efficiently predicting their combined impact on lift, drag, moments and center-of-pressure location. Incorporating unsteady effects—through URANS or LES—would capture transient loads during flap actuation in the transonic regime. Experimental validation in a subscale wind tunnel or shock-tube facility would further refine heat-transfer and boundary-layer models. Finally, integrating the aerodynamic database into a reentry guidance algorithm will allow closed-loop control laws to be tested in a flight-dynamics environment, closing the

loop between CFD, control-surface sizing, and trajectory optimisation for fully reusable spacecraft.

In addition, a rigorous examination of surface pressure or velocity (Fig. 11.2, 11.3) distributions and three-dimensional velocity vector fields is recommended to confirm that local flow features remain sufficiently linear and decoupled, thereby validating the applicability of the superposition methodology across the full envelope of flap and canard deflections.

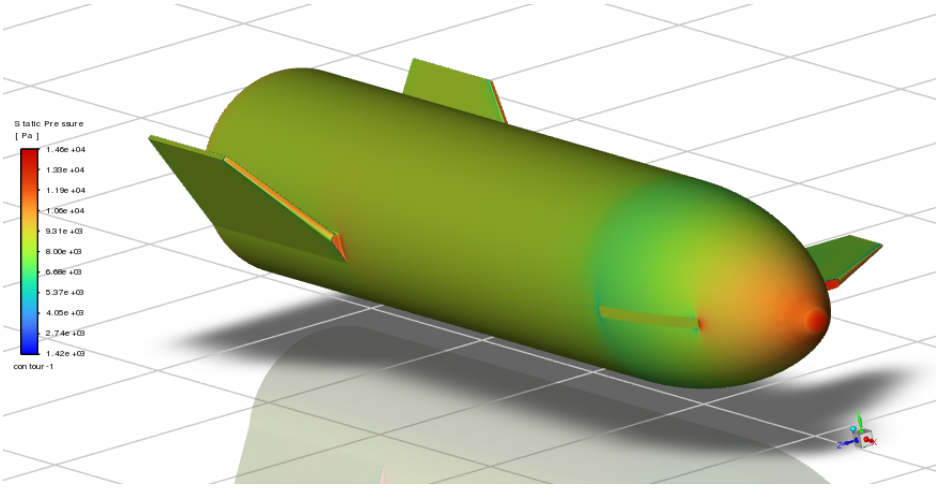


Figure 11.2. Pressure contours for AoA=0deg. fin 60deg canard60deg M=0.82

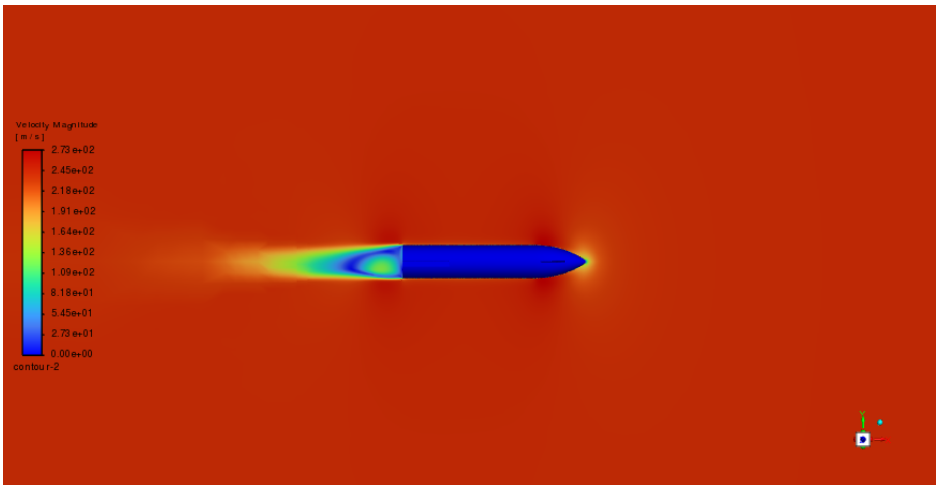


Figure 11.3. Velocity contours in z=0 plane for AoA=0deg. fin 60deg canard60deg M=0.82

References

[1] *Spacex falcon 9 launches fifth x-37b mission*, https://spaceflight101.com/spacex-falcon-9-launches-fifth-x-37b-mission/, [Online; accessed 30 December, 2023].

[2] *Aerospaceweb: Air-to-air missile design*, https://aerospaceweb.org/question/weapons/q0261.shtml, [Online; accessed 30 December, 2023].

List of Figures

1.1 Starship rocket configurations with future plans to develope 7
2.1 Starship rocket damaged fin closeup 9
4.1 Analyzed domain 11
5.1 Mesh created for the model 12
5.2 Denser mesh on cannards 13
5.3 Skewness and orthogonality of the mesh 14
6.1 Convergence of residuals and drag coefficient 16
9.1 Lift coefficient vs Mach graph 22
9.2 Moment coefficient vs Mach graph 23
9.3 Drag coefficient vs Mach graph 23
11.1 Iso-Surface AoA-0deg fin60deg canard60deg M=1.81 26
11.2 Pressure contours for AoA=0deg. fin 60deg canard60deg M=0.82 27
11.3 Velocity contours in z=0 plane for AoA=0deg. fin 60deg canard60deg M=0.82 . 27

List of Tables

5.1 Simulation results with different mesh resolutions. 14
6.1 Comparison of aerodynamic coefficients for opposing fin and canard angles. . 17
8.1 Flow conditions for selected Mach numbers 21

List of Appendices

1. Tables with obtained values 30

Appendix 1. Tables with obtained values

Case 1 Mesh independency studies

#cells	c_d	c_l
1.82E+06	0.637	0.118
2.77E+06	0.631	0.119
4.97E+06	0.617	0.115
7.00E+06	0.601	0.116

Case 2 Results

Mach	cd	cl	cz	cd/cl
0.29	0.44	0.72	0.92	0.62
0.66	0.45	0.72	0.93	0.62
1.00	0.59	0.58	1.25	1.02
1.36	0.50	0.37	1.07	1.36
1.92	0.37	0.18	0.81	2.03
2.62	0.30	0.16	0.67	1.83
3.32	0.24	0.15	0.53	1.62

Case 3 Results

M (0deg)	c_d	c_L	c_z
0.29	0.46	0.15	0.51
0.66	0.46	0.14	0.51
1.00	0.50	0.10	0.55
1.36	0.62	0.10	0.65
1.92	0.52	0.16	0.54
3.32	0.33	0.14	0.33

Case 3 Mesh independency studies

#cells	c_d	c_l
1.00E+06	0.398	0.145
2.04E+06	0.495	0.151
2.92E+06	0.475	0.167
3.82E+06	0.466	0.147
4.91E+06	0.439	0.153
5.21E+06	0.428	0.153
7.69E+06	0.435	0.142
8.69E+06	0.440	0.136
1.05E+07	0.410	0.141
1.08E+07	0.425	0.143

.